Paper

Significantly enhanced permittivity and energy density in dielectric composites with aligned $BaTiO_3$ lamellar structures

Received 00th January 20xx,
Accepted 00th January 20xx

DOI: 10.1039/x0xx00000x

Ru Guo[a▽], James Roscow[b▽], Chris R. Bowen[b], Hang Luo[a]*, Yujuan Huang[a], Yupeng Ma[a], Kechao Zhou[a] and Dou Zhang[a]*

Significant improvement of the permittivity and energy density will enable the miniaturization of dielectric capacitors and promote the integration for applications in electrical power and defense systems. In this work, lamellar composite architectures formed from aligned barium titanate ($BaTiO_3$) in an epoxy resin are fabricated using the freeze casting method. Due to the continuous coupling effect originated from the interconnected and highly oriented $BaTiO_3$ particles, this composite exhibits extremely high permittivity (ε_r = 1408) at 1 kHz, which is the highest value achieved in $BaTiO_3$/polymer composites reported so far and fits well to the parallel mode of the mixing rule. A finite element model is used to investigate the local electric field distributions in the $BaTiO_3$ laminar under the applied electric field parallel and perpendicular to the freezing direction, respectively. A high ratio value of discharge energy density per electric field, U_{dis}/E, ~ 0.033, is achieved due to the high electric displacement of D = 15.11 μC/cm^2 and discharge energy density of U_{dis} = 19.6×10^{-2} J/cm^3 achieved at a low electric field (6 kV/mm). This work provides an effective strategy of designing ceramic-polymer composite to realize high permittivity and energy density of capacitors for modern electrical and electronic industries.

Introduction

The energy crisis caused by the traditional fossil fuel consumption and environmental deterioration due to global warming has triggered global attention to smart energy production and storage solutions.[1-8] Among the various energy storage devices, such as solar cells, fuel cells and lithium batteries, there is growing interest in electrostatic capacitors for use in smart grids and pulsed power equipment due to their high discharge power density (~10^4-10^7 W/kg), long service time and low cost.[9-13] However, the relatively low energy density (~10^{-2}-10^{-1} Wh/kg) of capacitors currently limits their use in a broader range of applications that need to draw upon a large amount of total stored energy.[14-17] The maximum discharge energy density for a linear dielectric is given by:

$$U_{dis} = \frac{1}{2}\varepsilon_0\varepsilon_r E_b^2 \qquad (1)$$

where ε_0 and ε_r are the permittivity of free space (ε_0 = 8.854 x 10^{-12} F/m) and relative permittivity, respectively, and E_b is the breakdown strength of the material.[4, 18, 19] From equation (1) it is clear that the discharged energy density of a capacitor can be improved by increasing either the permittivity of the material or the breakdown strength. Composites have received increasing attention recently due to the potential for tuning the relevant electrical properties compared to the properties of the single phase constituents[20-24], whilst also providing an opportunity for improving the mechanical properties, e.g. offering a degree of mechanical flexibility, damage tolerance or toughness compared to monolithic ceramics.

Ferroelectric ceramics, such as $BaTiO_3$, $Ba(Zr_xTi_{1-x})O_3$, $Pb(Zr_{1-x}Ti_x)O_3$, and $Na_{0.5}Bi_{0.5}TiO_3$, are often used as a filler in polymer matrices due to their high permittivity.[25-29] The tape casting method has been commonly used to fabricate these composites by incorporating randomly dispersed ceramic fillers into the polymer matrix. In general, the enhancement of the composites' permittivity is largely limited compared with the low value of polymer matrix, even when the filler loading is at a high level, e.g. 50 vol.%.[3, 25, 30, 31] This is mainly ascribe to the weakened polarization effect resulting from the permittivity mismatch between ceramic fillers and polymer matrix, while the localized electric field applied in the high permittivity ceramic phase is relatively low.[32] Thence, it is a challenge to achieve a significant enhancement in permittivity while maintaining structural integrity in a ceramic-polymer composite.

A number of theoretical models[3, 5] (Supporting Information, Equation S1-5) for the effective permittivity of composites have been proposed based on experimental results and connectivity of the structure.[3, 33, 34] These include the *parallel and series models[33] that are specific cases of the Lichtenecker model*[3] in which the effective permittivity of a composite is given by:

$$\varepsilon^k = v_1\varepsilon_1^k + v_2\varepsilon_2^k \qquad (2)$$

where v is the volume fraction, ε is permittivity and k is a structure factor. When the two phases are ideally connected in series relative to the direction of applied field, k = -1, and when they are connected in parallel, k = 1. The parameter k is usually determined experimentally, and for randomly dispersed

[a] State Key Laboratory of Powder Metallurgy, Central South University, Changsha 410083, Hunan Province, China.
[b] Department of Mechanical Engineering, University of Bath, Bath BA2 7AY, United Kingdom.
†*E-mail: dzhang@csu.edu.cn, hangluo@csu.edu.cn
▽Dr. Ru Guo and Dr. James Roscow contributed equally to this work.
Electronic Supplementary Information (ESI) available: [details of any supplementary information available should be included here]. See DOI: 10.1039/x0xx00000x

polymer matrix composites, typically k < 0. The *Jayasundere-Smith model* and *Maxwell-Garnett model*[5] were proposed to consider the shape, size and distance of high permittivity fillers within a low permittivity matrix, and as such they sit below the k = 0 line of the Lichtenecker model. Based on the same principles, the Maxwell-Garnett model is only valid when the volume fraction of the filler v_f < 0.1, whereas the Jayasundere-Smith model has been adapted to consider higher filler volume fractions. Figure 1 shows the effective permittivity, normalized to that of the high permittivity phase, of $BaTiO_3$/polymer composites using the Lichtenecker, Jayasunder-Smith and Maxwell-Garnett models as a function of $BaTiO_3$ volume fraction. The models were calculated using measured values for the relative permittivity of barium titanate and epoxy, ε_r = 2270 and ε_r = 7.1, respectively, used to produce the composites investigated later in this paper (see Section 2 onwards). For the Lichtenecker model, three values of k have been used and related to the series (k = -1), parallel (k = 1), and an approximate transition from polymer matrix to ceramic matrix ($k \approx 0$) that we propose here. Dispersing ferroelectric powders in a polymer matrix tends to result in poor connectivity between the high permittivity ferroelectric particles, leading to local electric field concentrations in the low permittivity phase when an electric field is applied across the material. As a result, the effective permittivity of the composite is dominated by the low permittivity matrix.[29] This has been commonly observed in porous ferroelectric ceramics, such as those used for piezoelectric energy harvesting, whereby electric fields concentrate in the low permittivity pores.[35] As such, controlling the morphology and volume fraction of ferroelectric particle fillers has not enhanced significantly the permittivity of composites compared to that of the low permittivity matrix for energy storage applications.[36, 37]

Previous studies have demonstrated that the effective permittivity of a ceramic-polymer composite can be enhanced by aligning the high permittivity filler via electrospinning and uniaxial stretching methods.[28, 38-40] However, the relative permittivity of the composites tend to remain below ε_r = 100. Recently, Luo et al. designed a novel composite with a three-dimensional $BaTiO_3$ network and found a relatively high permittivity (ε_r = 200 at 1 kHz) and discharged energy density (U_{dis} = 16.3×10^{-3} J/cm^3 at 10 kV/mm),[33] whilst still being based on a polymer matrix. To achieve a high effective permittivity, it is beneficial to form a continuous ferroelectric phase, i.e. using an interconnected high permittivity ferroelectric ceramic matrix rather than a continuous low permittivity polymer phase, in order to move towards the parallel model, and above the $k \approx 0$ line in the Lichtenecker model, as shown in Figure 1.

Freeze casting is an effective strategy to form highly orientated ceramic matrix composites, which has been previously utilized effectively to produce porous piezoelectric ceramics and composites for sensing and energy harvesting.[41, 42, 43-46] During the freezing casting process, a suspension of ceramic powder in a solvent, often water, is directionally frozen. The ceramic phase is ejected by the solidification front of the solvent into lamellae between the ice crystals.[47] By controlling the cooling rate and temperature gradient during freezing, excellent control of the microstructure can be achieved.[48, 49] After freezing, the solidified solvent phase is removed by freeze drying, and the remaining powder structure is sintered to consolidate it into a continuous ceramic matrix with pores orientated to the freezing direction.[50] This porous ceramic structure can then be infiltrated with polymer to form the composite.

Using the freeze casting method, we have fabricated highly orientated porous barium titanite ceramics and infiltrated this matrix with an epoxy resin. Due to the highly aligned orientation of the $BaTiO_3$ phase, the relative permittivity of the composites reached to ε_r =1408 at 1 kHz with $BaTiO_3$ volume fraction, v_f = 59 vol%. Meanwhile, high electric displacement of 15.11 μC/cm^2 and discharge energy density of 19.6×10^{-2} J/cm^3 were achieved at low electric fields of 6 kV/mm, which were 10.1 and 6.5 times higher than composites with the randomly distributed $BaTiO_3$ particles in an epoxy matrix, fabricated for comparison. This work demonstrates that lamellar architectures, such as those obtained by the freeze casting process, are an effective route to achieve high permittivity and energy density in ceramic/polymer composites.

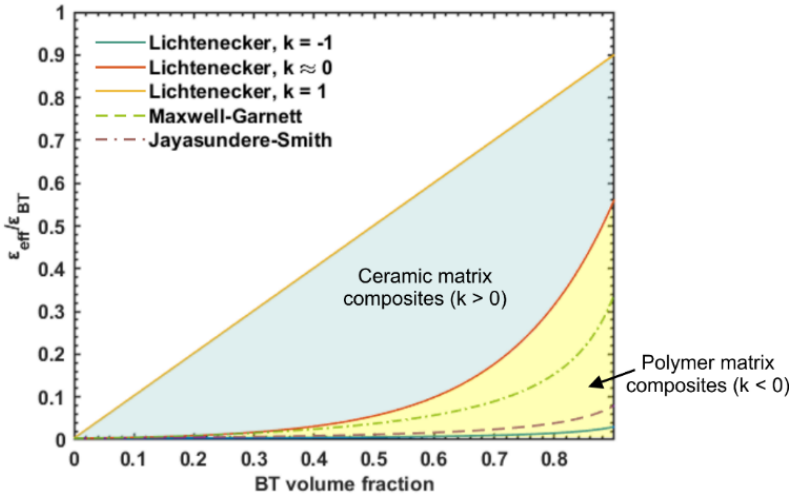

Paper

Figure 1. Effective permittivity of $BaTiO_3$/polymer composites, normalized to the permittivity of pure BT, as a function of $BaTiO_3$ volume fraction, as predicted by various models. Polymer matrix composites tend to result in an effective permittivity below the line k = 0 using the Lichtenecker model approach.

Experimental section

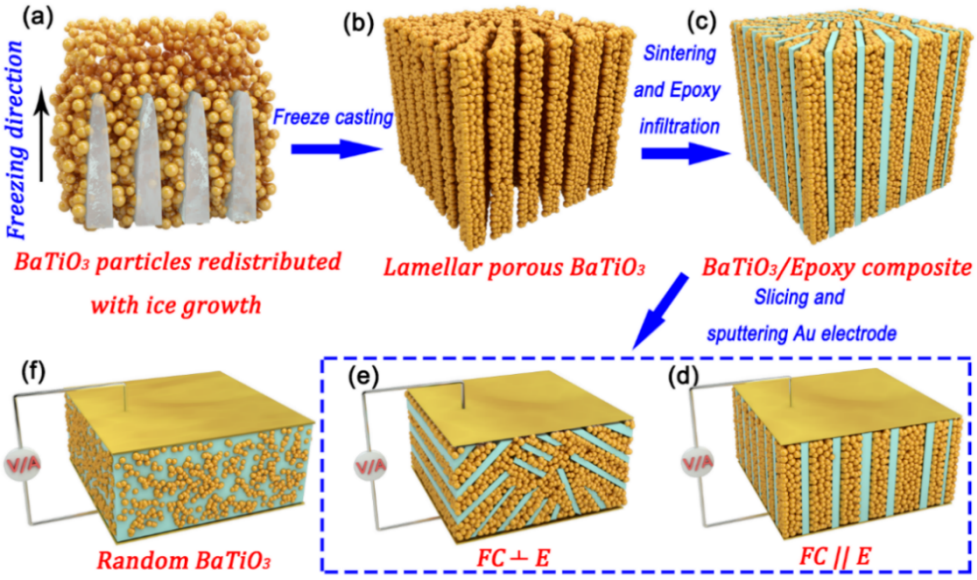

Raw materials

The raw materials used to fabricate the ceramic/polymer composites were $BaTiO_3$ powder with particle size of 0.5 μm (Shanghai Dianyang Industry Co. Ltd.), the Araldite 2020 epoxy resin (Huntsman), polyammonium acrylate (Highrun Chemical Co. Ltd.), and polyvinyl alcohol (Sinopharm, China). And the structure and composition information of $BaTiO_3$ powder were shown in Fig.S1(Supporting Information).

Freeze casting of porous $BaTiO_3$ ceramics

Deionized water, $BaTiO_3$ powder and a dispersant (polyammonium acrylate) were mixed to prepare suspensions with 10 vol.%, 20 vol.% and 30 vol.% solid loading. After ball milling for 24 h, 1 wt.% polyvinyl alcohol (based on the weight of the $BaTiO_3$ powder) was added to the suspension to act as a binder and stirred slowly for 12 h. The suspensions were directionally cooled by liquid nitrogen at 10 °C /min rates and then placed in the vacuum chamber (< 10 Pa) of a freeze-drier for 48 h to remove the ice. The porous green bodies were placed in a furnace and heated in air with a heating rate of 1 °C/min at 600°C for 2 h to burn out the organic additives and sintered at 1200 °C for 3 h.

The preparation of $BaTiO_3$/epoxy composites

The porous $BaTiO_3$ ceramics were immersed in a uniformly mixed resin of Araldite 2020 epoxy A/B component with mass ratio of 10:1.5. The samples were then evacuated in a vacuum to fully infiltrate the epoxy resin in the porous ceramic matrix. After being subjected to a vacuum for 12 h and cured at 80°C for 24 h, the $BaTiO_3$/epoxy composites were sectioned and ground to a thickness of ~1 mm. Two orientations of sample were investigated by sectioning samples parallel and perpendicular to the freezing direction. Finally, the surface of the samples was sputtered with gold electrodes for electrical characterization.

For comparison, $BaTiO_3$ powder was randomly dispersed in Araldite 2020 epoxy resin, and after stirring for 1 h, the film was scraped off on the substrate. The samples were kept under vacuum for 12 h and cured at 80°C for 24 h to obtain the $BaTiO_3$/epoxy composites with randomly distributed spherical filler particles. The detailed process of preparing $BaTiO_3$/epoxy composites is shown in Figure 2.

Characterization of composites

The morphology and microstructure of the samples were observed by scanning electron microscopy (SEM, JSM-6390). The frequency dependence of permittivity and dielectric loss at room temperature were measured using an Agilent 4294A LCR meter with a frequency range from 1 kHz to 10 MHz. The polarization-electric field hysteresis loops of the composites were performed at 10 Hz by a TF analyzer 2000 ferroelectric polarization tester (aixACT, Germany) with Delta 9023 furnace in a silicone oil bath to avoid electrical discharge that would otherwise occur during testing in air. The energy storage performance of the composites was calculated according to the hysteresis loops.

Simulations

Two-dimensional electrostatic finite element simulations were used to assess the local electric field distributions in the $BaTiO_3$/epoxy samples under an applied electric field. Geometries were created from scanning electron micrographs (SEMs) of the microstructures of the 10 vol.% freeze cast samples at different orientations to the freezing direction (i.e.

parallel and perpendicular), which had a barium titanate volume fraction, v_f ~ 0.24 after sintering and infiltrating with epoxy. The SEMs were binarized and converted into a 500 x 500 mesh of square elements and the phases were assigned the properties of barium titanate (ε_r =2270, determined experimentally) and epoxy (ε_r = 7.1, determined experimentally). A static electric field was applied across the model and the distribution of local field magnitude and angle in each element was analyzed as a tool to interpret the experimental results. The SEM images used to create the models are shown in Figure 3 (a) and (d).

Figure 2. Schematic of $BaTiO_3$/epoxy composites fabrication process.

Results and discussion

Figure 3 shows the microstructure of the $BaTiO_3$/epoxy composite in the perpendicular and parallel freezing direction with the $BaTiO_3$ loading level of 10 vol.%, 20 vol.% and 30 vol.% in the initial suspension, respectively. The morphologies of the composites are shown in Figure 3 where the thickness of the $BaTiO_3$ layer increased with increasing BaTiO3 loading level from 10 vol.% to 30 vol.%; the thicknesses of the $BaTiO_3$ and epoxy lamellar are summarized in Table 1. This tendency can be ascribed to the high viscosity of the suspension due to the high $BaTiO_3$ fraction which blocks and reduces the ice growth rate. The $BaTiO_3$ particles are therefore unable to be redistributed effectively to populate the regions between growing ice crystals, eventually leading to an increase in the thickness of the $BaTiO_3$ layer.[43] The relative density, ρ_{rel}, of the barium titanate increased with initial solid loading content, from ρ_{rel} = 0.24 for the 10 vol.% solid loaded suspension to ρ_{rel} = 0.59 for the 30 vol.% solid loading. The ρ_{rel} values correspond to the $BaTiO_3$ volume fraction, v_f, in the final composite, see Table 1. The difference between the $BaTiO_3$ volume fraction of the final composite and initial suspension was due to the densification of the ceramic channels during to sintering. In terms of overall morphology, the composites had a pseudo 2-2 connectivity composed of planes of an aligned $BaTiO_3$ ceramic matrix and epoxy.

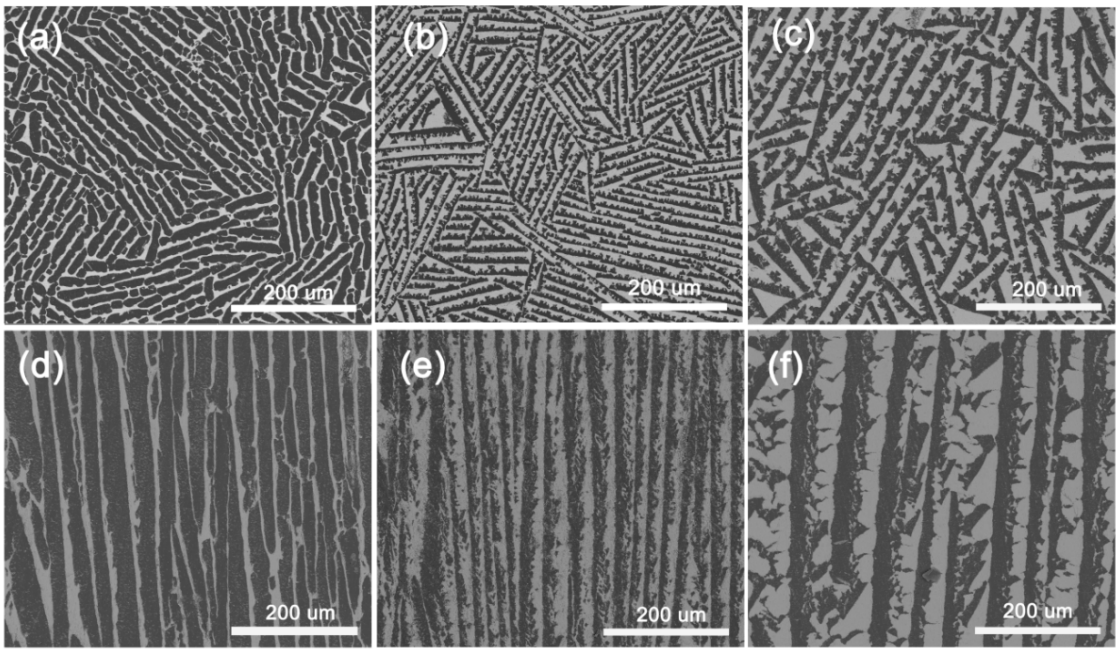

Figure 3 SEM images of the $BaTiO_3$/epoxy composites in the perpendicular freezing direction with varying $BaTiO_3$ volume fractions, (a) 0.24, (b) 0.40, (c) 0.59, and in the parallel freezing direction with (d) 0.24, (e) 0.40, and (f) 0.59, respectively, in final composites.

Table 1. Morphological parameters of the freeze cast $BaTiO_3$/epoxy composite.

$BaTiO_3$ solid loading (vol.%)	$BaTiO_3$ volume fraction (v_f) of final composite	Thickness of $BaTiO_3$ layer (μm)	Thickness of epoxy resin (μm)
10	0.24 ± 0.02	10.6 ± 2.2	33.8 ± 4.9
20	0.40 ± 0.02	20.9 ± 2.7	22.1 ± 3.5
30	0.59 ± 0.03	45.3 ± 4.5	24.3 ± 3.6

The frequency dependence of the permittivity and dielectric loss of the $BaTiO_3$/epoxy composites was measured from 1 kHz to 1 MHz at room temperature. As presented in Figure 4, the permittivity of the all samples decreased slightly with increasing frequency, which was attributed to the switching of the interfacial polarization between the two phases lagging behind the voltage signal at high frequency.[51] The permittivity increased with increasing volume fraction of barium titanate, shown in Figure 4 for (a) parallel, (b) perpendicular and (c) random particle distribution. The permittivity of composites with an electric field parallel to the freezing direction at $BaTiO_3$ fractions, v_f = 0.24, 0.40, and 0.59 at 1 kHz were ε_r = 427, 793, and 1408, respectively. Meanwhile, the permittivity of the composite with an electric field perpendicular to freezing direction at corresponding $BaTiO_3$ fractions were ε_r = 214, 518, and 999, respectively, and that of the composite with a random $BaTiO_3$ particle distribution were much lower at ε_r = 38, 66, and 95, respectively. The dielectric properties of $BaTiO_3$/epoxy composite are summarized in Table 2. In addition, the evolution of dielectric properties as a function of temperature for the $BaTiO_3$/epoxy composites was shown in Figure S5(Supporting Information). Temperature dependence of permittivity have been measured from 25°C to 150°C. The permittivity of the composites remains relatively high in the whole temperature range, and which reaches the largest value at the curie temperature. Figure 4(d) illustrates the failure probability of breakdown strengths analysed with a two-parameter Weibull distribution for the $BaTiO_3$ ceramic, epoxy resin and its composites. The magnitude of E_0 represents the breakdown strength of the material at the cumulative failure probability of 63.2%, calculated from the function:

$$P(E) = 1-\exp(-(E/E_0)^{\beta}) \quad (3)$$

where β was the Weibull modulus associated with the linear regressive fit of the distribution; a higher value of β represents less scattering. The breakdown strength of the $BaTiO_3$ ceramic and epoxy resin was 7.3 kV/mm and 54.5 kV/mm, respectively. The breakdown strengths of the v_f = 0.59 $BaTiO_3$ fraction freeze cast $BaTiO_3$/epoxy composites for electric fields applied parallel and perpendicular to the freezing direction were found to be E_0 = 20.5 kV/mm and E_0 = 26.7 kV/mm, respectively, and that of the composite with a random $BaTiO_3$ particle distribution was measured as E_0 = 34.4 kV/mm. These results demonstrate that the breakdown strength of the $BaTiO_3$ ceramic/polymer composites can be improved compared to the single phase $BaTiO_3$ ceramic (E_0 = 7.3 kV/mm)

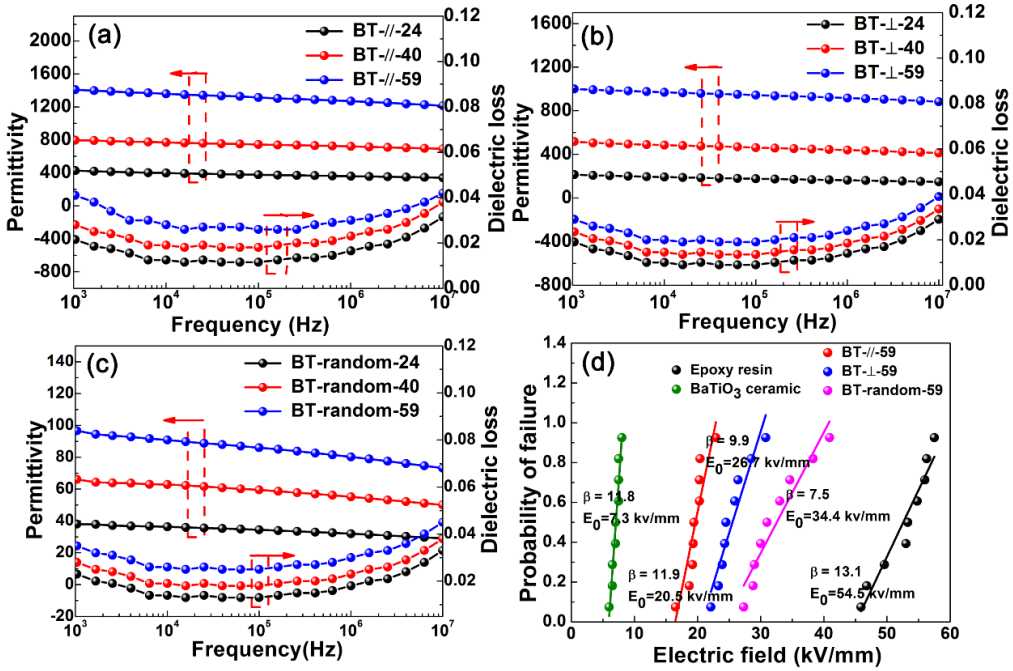

Figure 4. Frequency dependence of the permittivity and dielectric loss of the $BaTiO_3$/epoxy composites with $BaTiO_3$ fractions of v_f = 0.24, 0.40 and 0.59. The electric field was applied (a) parallel, and (b) perpendicular relative to the freezing direction of the composites. (c) Field dependent permittivity and dielectric loss of the composites with $BaTiO_3$ particles randomly distributed in epoxy resin. (d) Failure probability of dielectric breakdown deduced from Weibull distribution for samples.

Table 2. Definition of sample names and the summary of dielectric properties. (e.g. "BT-//-24" represents the composite with $BaTiO_3$ fractions of v_f = 0.24 was tested under the electric field which parallel to the freezing direction.)

Sample name	Applied field direction relative to freezing direction	$BaTiO_3$ volume fraction (v_f) of final composite	Relative permittivity (1 kHz)	Dielectric loss (1 kHz)
BT-//-24	parallel	0.24 ± 0.02	427	0.028
BT-//-40	parallel	0.40 ± 0.02	793	0.031
BT-//-59	parallel	0.59 ± 0.03	1408	0.042

BT-⊥-24	perpendicular	0.24 ± 0.02	214	0.023
BT-⊥-40	perpendicular	0.40 ± 0.02	518	0.028
BT-⊥-59	perpendicular	0.59 ± 0.03	999	0.041
BT-random-24	--	0.24 ± 0.02	37	0.021
BT-random-40	--	0.40 ± 0.02	66	0.028
BT-random-59	--	0.59 ± 0.03	95	0.035

To understand the dielectric properties of the various composite structures, finite element simulations were used to assess the local electric field distributions in the 10 vol.% solid loaded freeze cast composites ($BaTiO_3$ v_f = 0.24, see Table 1). Contour plots of local field magnitude for the parallel and perpendicular aligned structures are shown in Figure 5 (a) and (b), respectively, separated into barium titanate and epoxy. The corresponding distributions of local electric field magnitude, relative to the applied field, are shown in Figure 5 (c) and (d), again separated by phase. Since the local electric field in each element is a vector characterized by a magnitude and an angle, the distribution of local field angles for both parallel and perpendicular orientations are shown in Figure 5 (e) and (f), respectively. From the field distributions, it can be seen that aligning the anisometric structure to the applied field (Figure 5(a)) leads to higher average electric fields in both the barium titanate and epoxy phases compared to the perpendicular orientation, shown in Figure 5(b). The electric field tends to concentrate in the low permittivity matrix, which leads to lower effective permittivity in composites where the high permittivity phase is less interconnected in the direction of the applied field; this occurs more readily when the field is applied perpendicular

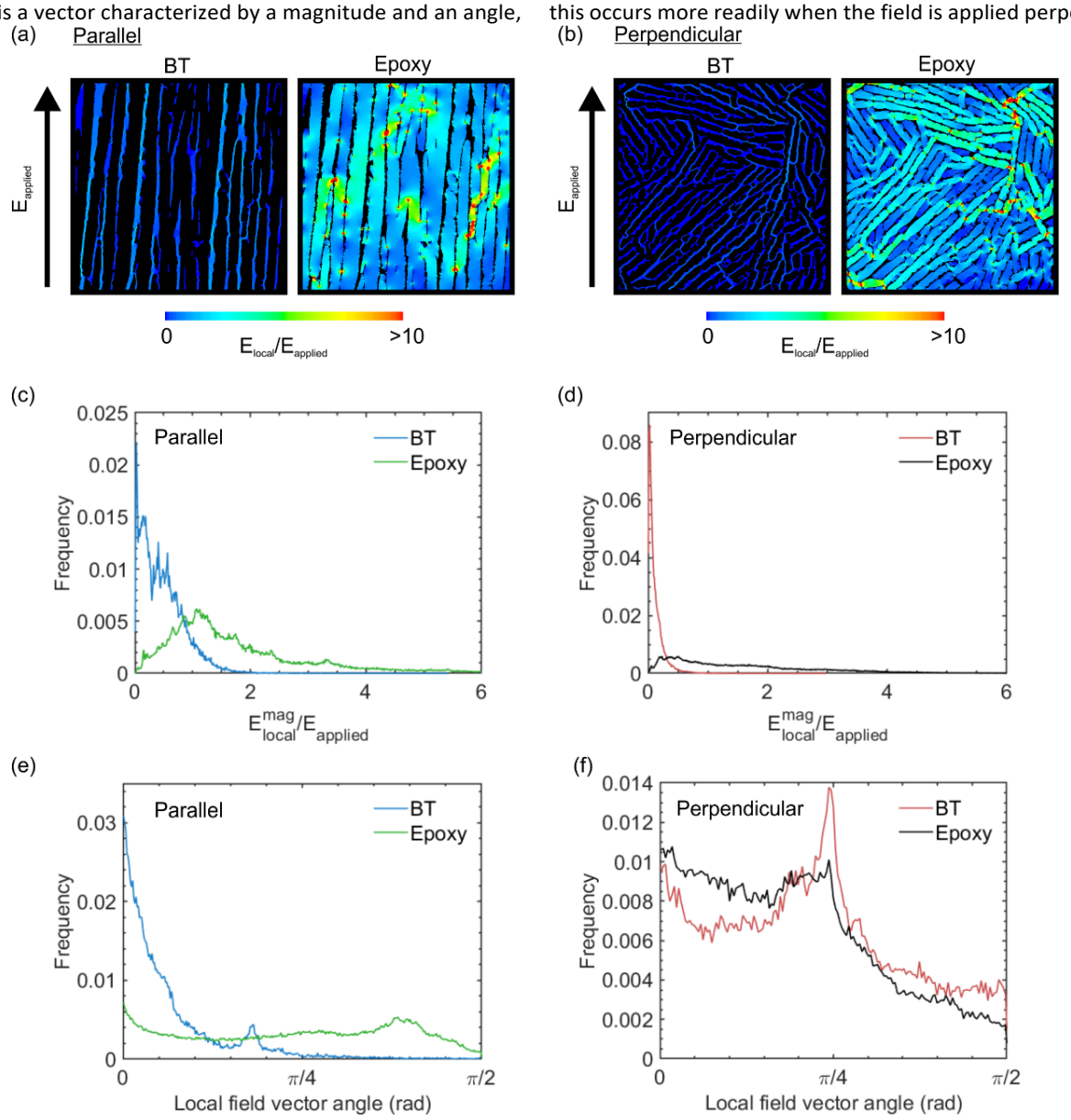

to the freezing direction. In order to achieve a high effective permittivity in a composite, the structure needs to promote local electric fields which are similar in magnitude to the applied field within the high permittivity phase, otherwise the effect is analogous to applying a field across two capacitors connected in series, whereby the overall capacitance is dominated by the low capacitance (or low permittivity) component.

Figure 5. Local electric field magnitude contour plots are shown for freeze cast $BaTiO_3$/epoxy composites with a $BaTiO_3$ $v_f = 0.24$ with field applied (a) parallel to and (b) perpendicular to the freezing direction. The corresponding distributions of local electric field magnitude for parallel and perpendicular are shown in (c) and (d), respectively. The distribution of local field vector angles relative to the direction of the applied field are shown in (e) and (f) for parallel and perpendicular composites, respectively. The data have been separated into individual phases.

In both the parallel and perpendicular cases, it can be seen that the electric field concentrates in the low permittivity epoxy phase (see green and red regions in Figure 5(a) and 5(b)), thereby leading to average local fields that are higher than the applied field. The corresponding distributions of local electric field magnitude for parallel and perpendicular in Figure 5(c) and 5(d), respectively show that there is a larger area fraction where the local field is greater than the applied field (i.e. $E_{local}/E_{applied}$ >1) for the parallel system compared to the perpendicular system. These occur because the $BaTiO_3$ phase is discontinuous in the direction of the applied field, leading to high field concentrations in the epoxy that infiltrates into the ceramic lamellae. Improving the freeze casting process to achieve a more continuous lamellae architecture may reduce these field concentrations, which from the model presented here are potentially weak points, or defects, in the structure that could initiate dielectric breakdown. As a result of the field concentration in both cases, it would be expected to observe breakdown at a lower field than the single phase polymer, as has been observed previously in a number of studies, and demonstrated in Figure 4(d). Similarly, the composite in which the structure was aligned perpendicular to the freezing direction was found to have a higher breakdown strength than the parallel composite, as the concentrations in the both the $BaTiO_3$ and epoxy phase are less severe, as can be seen by comparing Figure5 (c) and Figure 5 (d).

The distribution of local field vector angles relative to the direction of the applied field are shown in Figure 5(e) and Figure 5(f) for parallel and perpendicular composites, respectively. It can be seen that the perpendicular structure appears to disperse the local field vector away from the axis of applied field more so than in the structure aligned parallel, as can be seen by comparing Figure 5 (e) and (f). This may also promote a higher breakdown strength in the perpendicular composite relative to the parallel structures by increasing the length of the breakdown path, as observed experimentally (see Figure 4(d)).

Figure 6a shows the effective permittivity of the $BaTiO_3$/epoxy composite in this study and the value calculated by *Lichtenecker model*, indicating a good match between the both. As presented, the $BaTiO_3$/epoxy composites where the electric field applied parallel and perpendicular to the freezing direction gave the k value of 0.92 and 0.60, respectively. The randomly dispersed BT in epoxy has a k value less than 0 (~-0.18), which also exhibits relatively good fit with Jayasundere-Smith model. Meanwhile, it is worth mentioning that the composite with $BaTiO_3$ aligned in the lamellar architecture prepared via freeze casting method exhibits high permittivity, which is the highest value achieved in $BaTiO_3$/polymer composites reported so far and fits well to the parallel mode of the mixing rule, to the best of our knowledge. Figure 6b summarizes the permittivity and dielectric loss of two typical composites: i.e. $BaTiO_3$/epoxy-based composites and composites of aligned filler. Correspondingly, the volume fraction, mass or height ratio for each system were provided to make comparison. As shown in Figure 6b, the composite at $BaTiO_3$ filler $v_f = 0.59$ in our work with freezing direction parallel to electric field achieved the highest permittivity while maintaining dielectric losses at a low level and improving the breakdown strength compared to pure $BaTiO_3$, which are beneficial for enhancing the energy density and energy efficiency of composites.

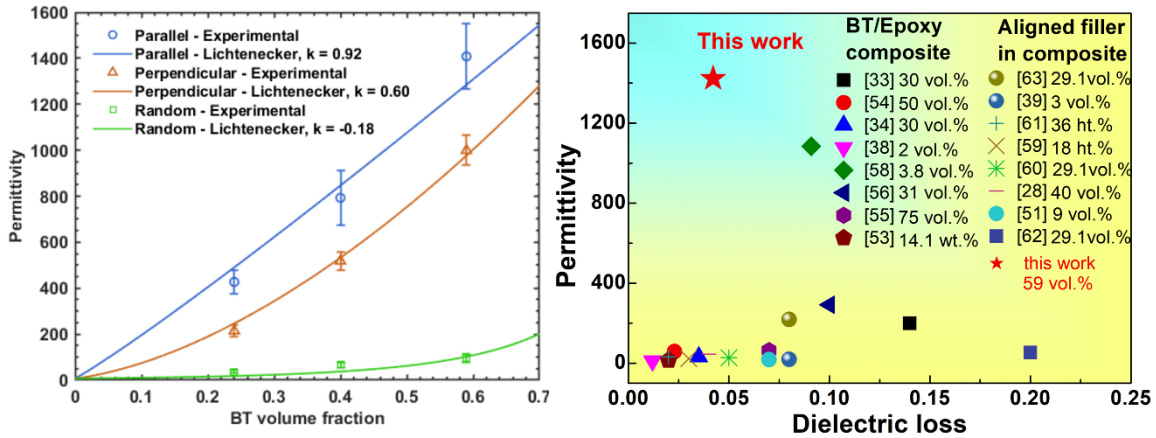

Figure 6. (a) *Lichtenecker model* to describe the relationship between permittivity and $BaTiO_3$ fraction in two-component composites.[33] The dots represent the permittivity value of the present study versus the $BaTiO_3$ fraction in the composites. (b) Summary of permittivity and dielectric loss of $BaTiO_3$/epoxy resin composites and that of the composites with aligned filler reported in the literature.[28, 33, 34, 38, 39, 51, 53-63]

Figure 7 a, b and c show the electric polarization-electric field (D–E) loops measured at 10 Hz and room temperature, corresponding to the electric fields applied parallel and perpendicular to the freezing direction of aligned $BaTiO_3$ composites, and the composites with randomly distributed $BaTiO_3$ particles, respectively. The maximum electric displacement of all three types of composites increased with increasing $BaTiO_3$ volume fractions. In addition, it was found that the composites with lamellar architectures prepared by the freeze casting method demonstrated superior electric displacements compared to random $BaTiO_3$ composite. For instance, the electric displacement of the polymer matrix composite with v_f = 0.59 of $BaTiO_3$ particles was only D = 1.5 μC/cm^2 under the test electric field of 6 kV/mm, while the freeze cast composites with the same $BaTiO_3$ volume fraction had electric displacements of D = 11.89 μC/cm^2 and D = 15.11 μC/cm^2 for an electric field applied perpendicular and parallel to the freezing direction at the same conditions, which were 7.9 and 10.1 times higher, respectively. According to the equation:

$$\mathrm{D} = \varepsilon_0 \varepsilon_r \mathrm{E} \qquad (4)$$

the enhanced electric displacements were attributed to higher permittivity of such ceramic matrix composites prepared by freeze casting. The discharged energy density calculated from the *D–E* loops based on the integral by equation at various electric fields are illustrated in Fig. 7(d):

$$U_{dis} = \int E dD \qquad (5)$$

The discharged energy density obtained in the freeze cast composite at a $BaTiO_3$ fraction of v_f = 0.59 was U_{dis} = 18.1×10^{-2} J cm^{-3} when the field was applied perpendicular to the freezing direction and U_{dis} = 19.6×10^{-2} J cm^{-3} when parallel to the lamellae, corresponding to improvement of 503% and 553% compared with the composite with randomly distributed filler particles (U_{dis} = 3.0×10^{-2} J cm^{-3}), respectively. These improvements demonstrate that lamellar ceramic matrix architecture is an effective way to achieve high energy densities under low applied electric fields.

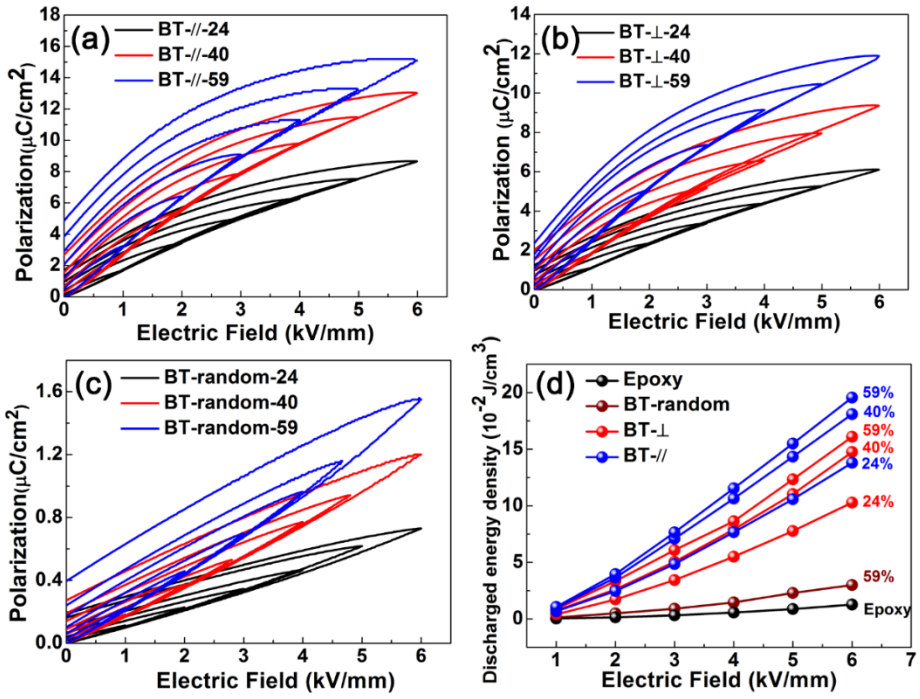

Figure 7. Electric displacements electric field (*D–E*) loop of the composite with test electric field (a) parallel, (b) perpendicular to the freezing direction, and (c) $BaTiO_3$ particles randomly distributed in epoxy resin. (d) The discharged energy density (U_{dis}) of the various composite structures investigate, for varying $BaTiO_3$ volume fractions as a function of electric field.

Table 3 summarizes the performance of some typical dielectric composites with aligned filler and shows the higher electric displacements of the composites fabricated in this work compared with the other composites. The ratio of the discharged energy density to the electric field was also superior to those of composites with aligned filler in PVDF or epoxy resin matrix. This suggests that the composites obtained in this study are expected to be high energy density capacitors in the field of low operating voltage. In addition, the bending strength of the composites were tested by three-point bending method (details are shown in Fig. S6, Supporting Information) to show the mechanical properties of the composites. The results showed that the bending strength of composite BT-random-59, BT-//-59, BT-⊥-59 are 55.79, 68.21, 75.45MPa, respectively, which were higher than that of the $BaTiO_3$ ceramic and epoxy resin of 30.12 and 44.60 MPa, respectively.

Table 3. Comparison of maximum electric displacements and discharged energy density at applied electric field for typical dielectric composites with aligned filler.

Filler	Matrix	E (kV/mm)	Max. electric displacement ($\mu C/cm^2$)	U_{dis} (J/cm^3)	$Udis/E$ Value	Ref.
TiO_2	PVDF	340	8.57	10.62	0.031	[61]
TiO_2	PVDF	505	10.66	8.9	0.017	[60]
PZT	PVDF	15	0.61	4.30×10^{-2}	0.003	[28]
TiO_2	P(VDF-HFP)	509	8.7	15.05	0.030	[51]
TiO_2@PZT	PVDF	550	7.8	12.6	0.025	[62]
$BaTiO_3$	Epoxy	10	0.347	1.57×10^{-2}	0.002	[56]
$BaTiO_3$	Epoxy	10	0.7	1.60×10^{-2}	0.002	[33]
Epoxy	$BaTiO_3$	6	15.11	19.6×10^{-2}	0.033	This work (parallel)
Epoxy	$BaTiO_3$	6	11.89	18.1×10^{-2}	0.030	This work (perpendicular)
$BaTiO_3$	Epoxy	6	1.5	3.0×10^{-2}	0.005	This work (random)

Conclusion

In summary, highly aligned lamellar barium titanate ($BaTiO_3$) architectures were fabricated via freeze casting, prior to sintering and infiltrating with epoxy resin to form $BaTiO_3$/epoxy composites. Composites were prepared by sectioning the $BaTiO_3$ parallel and perpendicular to the freezing direction to obtain different morphologies; the volume fraction of the barium titanate phase was adjusted by controlling the solid loading in the freeze casting process. Randomly dispersed polymer matrix composites were fabricated for comparison. Compared with the randomly distributed barium titanate composites, the permittivity of the composites with aligned $BaTiO_3$ structures were significantly higher at the same volume fraction (e.g. ε_r = 1408 compared to ε_r = 95 at $BaTiO_3$ volume fraction, v_f = 0.59). The composites with $BaTiO_3$ lamellae aligned to the direction of applied field had a higher permittivity than those with structures aligned perpendicular to the direction of applied field at the same volume fraction (ε_r = 1408 compared to ε_r = 999 at v_f = 0.59). However, the composites where the field was applied perpendicular relative to the freezing direction had higher breakdown strengths compared to the parallel samples, which were 20.5 kV/mm and 26.7 kV/mm, respectively for v_f = 0.59, although these were lower than the randomly dispersed composites (34.4 kV/mm) at a similar volume fraction.

Meanwhile, a high electric displacement of 15.11 $\mu C/cm^2$ and discharge energy density of U_{dis} = 19.6×10^{-2} J/cm^3 were achieved at low electric fields, i.e., 6 kV/mm, which was higher than the epoxy matrix composites at the same volume fraction of $BaTiO_3$ (electric displacement of 1.5 $\mu C/cm^2$ and discharge energy density of U_{dis} = 3.0×10^{-2} J/cm^3). The enhancement in energy storage capabilities indicates that the construction of a lamellar ceramic architecture is an effective method to obtain high dielectric properties and energy density of composites. This work provides a feasible avenue to design improved energy storage materials and is promising for the application of dielectric composites in modern electrical and electronic industries.

Conflicts of interest

There are no conflicts to declare.

Acknowledgements

This work was financially supported by the National Natural Science Foundation of China (51672311), the Hunan Natural Science Foundation (2019JJ40349), China Postdoctoral Science Foundation (2017M620353), Special Funding for the Postdoctoral Science Fund of China (2018T110840) and the State Key Laboratory of Powder Metallurgy, Central South University, Changsha, China.

References

1. L. Qi, C. Lei, M. R. Gadinski, S. Zhang, G. Zhang, H. Li, A. Haque, L. Q. Chen, T. Jackson, Q. Wang, *Nature*, 2015, 523, 576.
2. Y. Yang, J. He, Q. Li, L. Gao, J. Hu, R. Zeng, J. Qin, S. X. Wang, Q. Wang, Nature Nanotechnology 2019, 14, 151-155.
3. Z. M. Dang, J. K. Yuan, J. W. Zhai, T. Zhou, S. T. Li, G. H. Hu, *Progress in Materials Science*, 2012, 57, 660-723.

4. Z. Yao, Z. Song, H. Hao, Z. Yu, M. Cao, S. Zhang, M. T. Lanagan, H. Liu, *Advanced Materials*, 2017, 29, 1601727.
5. Prateek, V. K. Thakur, R. K. Gupta, *Chemical Reviews*, 2016, 116, 4260-4317.
6. Y. Zhang, C. Zhang, Y. Feng, T. Zhang, Q. Chen, Q. Chi, L. Liu, G. Li, Y. Cui, X. Wang, Z. Dang, Q. Lei, *Nano Energy*, 2019, 56, 138-150.
7. X. Huang, B. Sun, Y. Zhu, S. Li and P. Jiang, *Progress in Materials Science,* 2019, 100, 187-225.
8. L. Yang, X. Kong, F. Li, H. Hao, Z. Cheng, H. Liu, J. F. Li, S. Zhang, *Progress in Materials Science*, 2019, 102, 72-108.
9. X. Zhang, J. Jiang, Z. Shen, Z. Dan, M. Li, Y. Lin, C. W. Nan, L. Chen, Y. Shen, *Advanced Materials*, 2018, 30, 1707269.
10. S. Luo, J. Yu, S. Yu, R. Sun, L. Cao, W. H. Liao, C. P. Wong, *Advanced Energy Materials,* 2018, 1803204
11. Z. H. Shen, J. J. Wang, Y. Lin, C. W. Nan, L. Q. Chen, Y. Shen, *Advanced Materials*, 2018, 30, 1704380.
12. X. Zhang, B. W. Li, L. Dong, H. Liu, W. Chen, Y. Shen, C.W. Nan, *Advanced Materials Interfaces*, 2018, 5, 1800096.
13. Y. Wang, L. Wang, Q. Yuan, C. Jie, Y. Niu, X. Xu, Y. Cheng, B. Yao, Q. Wang, W. Hong, *Nano Energy*, 2018, 44, 364–370.
14. F. Liu, Q. Li, J. Cui, Z. Li, G. Yang, Y. Liu, L. Dong, C. Xiong, H. Wang, Q. Wang, *Advanced Functional Materials*, 2017, 27, 1606292.
15. Z. Pan, B. Liu, J. Zhai, L. Yao, K. Yang, B. Shen, *Nano Energy*, 2017, 40, 587-595.
16. Y. Xie, Y. Yu, Y. Feng, W. Jiang, Z. Zhang, *ACS applied materials & interfaces*, 2017, 9, 2995-3005.
17. H. Luo, S. Chen, L. Liu, X. Zhou, C. Ma, W. Liu, D. Zhang, *ACS Sustainable Chemistry & Engineering*, 2019, 7, 3145-3153.
18. Z. Pan, M. Wang, J. Chen, S. Bo, J. Liu, J. Zhai, *Nanoscale*, 2018, 10, 16621-16629.
19. Y. Wang, L. Wang, Q. Yuan, Y. Niu, C. Jie, Q. Wang, W. Hong, *Journal of Materials Chemistry A*, 2017, 5, 10849-10855.
20. G. Wang, X. Huang, P. Jiang, *ACS applied materials & interfaces*, 2017, 9, 7547-7555.
21. X. Huang, P. Jiang, *Advanced Materials*, 2015, 27, 546-554.
22. Y. Wang, J. Cui, Q. Yuan, Y. Niu, Y. Bai, H. Wang, Advanced Materials. 2015, 27, 6658-6663.
23. Z. Pan, J. Zhai, S. Bo, *Journal of Materials Chemistry A*, 2017, 5, 15217-15226.
24. H. Luo, Z. Wu, X. Zhou, Z. Yan, K. C Zhou, D. Zhang., *Composites Science & Technology*, 2018, 160, 237-244.
25. G. Wang, X. Huang, P. Jiang, *ACS applied materials & interfaces*, 2015, 7, 18017-18027.
26. X. Lin, P. H. Hu, Z. Y. Jia, S. M. Gao, *Journal of Materials Chemistry A*, 2016, 4, 2314-2320.
27. Y. Zhang, Q. Chi, L. Liu, T. Zhang, C. Zhang, Q. Chen, X. Wang, Q. Lei, *ACS Applied Energy Materials*, 2018, 1, 6320-6329.
28. H. Tang, Y. Lin, H. A. Sodano, *Advanced Energy Materials*, 2012, 2, 393-393.
29. H. Luo, J. Roscow, X. Zhou, S. Chen, X. Han, K. Zhou, D. Zhang, C. R. Bowen, *Journal of Materials Chemistry A*, 2017, 5, 7091-7102.
30. H. Luo, D. Zhang, C. Jiang, X. Yuan, C. Chen, K. Zhou, *ACS applied materials & interfaces*, 2015, 7, 8061-8069.
31. H. Luo, C. Ma, X. Zhou, S. Chen, D. Zhang, *Macromolecules*, 2017, 50, 5132-5137.
32. H. Luo, X. Zhou, C. Ellingford, Y. Zhang, S. Chen, K. Zhou, D. Zhang, C. R. Bowen, C. Wan, *Chemical Society Reviews*, 2019, DOI: 10.1039/c9cs00043g.
33. S. Luo, Y. Shen, S. Yu, Y. J. Wan, W. H. Liao, R. Sun, C. Wong, *Energy & Environmental Science*, 2017, 10, 137-144.
34. S. K. Dong, C. Baek, H. J. Ma, D. K. Kim, *Ceramics International*, 2016, 42, 7141-7147.
35. J. I. Roscow, R. W. C. Lewis, J. Taylor, C. R. Bowen, *Acta Materialia*, 2017, 128, 207-217.
36. Y. Zhang, T. Zhang, L. Liu, Q. Chi, C. Zhang, Q. Chen, Y. Cui, X. Wang, Q. Lei, *The Journal of Physical Chemistry C*, 2018, 122, 1500-1512.
37. B. Xie, Q. Zhang, L. Zhang, Y. Zhu, X. Guo, P. Fan, H. Zhang, *Nano Energy*, 2018, 54, 437-446.
38. Á. HA, L. A. Ramajo, M. S. Góes, M. M. Reboredo, M. S. Castro, R. Parra, *ACS applied materials & interfaces*, 2013, 5, 505-510.
39. B. Xie, H. Zhang, Q. Zhang, J. Zang, C. Yang, Q. Wang, M. Y. Li, S. Jiang, *Journal of Materials Chemistry A*, 2017, 5, 6070-6078.
40. Y. Guo, S. Batra, Y. Chen, E. Wang, M. Cakmak, *ACS applied materials & interfaces*, 2016, 8, 18471-18480.
41. J. Roscow, Y. Zhang, M. Kraśny, R. Lewis, J. Taylor, C. Bowen, *Journal of Physics D: Applied Physics*, 2018, 51, 225301.
42. Y. Zhang, M. Xie, J. Roscow, Y. Bao, K. Zhou, D. Zhang, C. R. Bowen, *Journal of Materials Chemistry A*, 2017, 5, 6569-6580.
43. Z. Yan, Y. Bao, Z. Dou, C. R. Bowen, *Journal of the American Ceramic Society*, 2015, 98, 2980-2983.
44. R. Guo, C. A. Wang, A. K. Yang, *Journal of the European Ceramic Society*, 2011, 31, 605-609.
45. S. H. Lee, S. H. Jun, H. E. Kim, Y. H. Koh, *Journal of the American Ceramic Society*, 2010, 91, 1912-1915.
46. M. Xie, Z. Yan, M. J. Kraśny, C. Bowen, H. Khanbareh, N. Gathercole, *Energy & Environmental Science*, 2018, 11, 2919-2927.
47. S. Deville, E. Saiz, R. K. Nalla, A. P. Tomsia, *Science*, 2006, 311, 515-518.
48. S. Deville, E. Saiz, A. P. Tomsia, *Acta Materialia*, 2007, 55, 1965-1974.
49. M. C. Gutiérrez, M. L. Ferrer, F. D. Monte, *Chemistry of Materials*, 2008, 20, 634-648.
50. Y. Yao, X. Zhu, X. Zeng, R. Sun, J. B. Xu, C. P. Wong, *ACS applied materials & interfaces*, 2018, 10, 9669−9678.
51. S. Liao, Z. Shen, P. Hao, Z. Xin, S. Yang, Y. Lin, C. Nan, *Journal of Materials Chemistry C*, 2017, 5, 12777-12784.
52. W. T. Scott, *American Journal of Physics*, 1998, 44, 611-616.
53. L. Lei, S. Zheng, *Journal of Applied Polymer Science*, 2015, 133, 43322.
54. J. Xu, S. Bhattacharya, P. Pramanik, C. P. Wong, *Journal of Electronic Materials*, 2006, 35, 2009-2015.
55. Z. M. Dang, Y. F. Yu, H. P. Xu, J. Bai, *Composites Science & Technology*, 2008, 68, 171-177.
56. Z. Zheng, S. Luo, S. Yu, Z. Guan, S. Rong, C. P. Wong, *Materials & Design*, 2018, 142, 106-113.
57. L. Qi, B. I. Lee, S. H. Chen, W. D. Samuels, G. J. Exarhos, *Advanced Materials*, 2010, 17, 1777-1781.
58. W. Ying, Z. Wang, S. Xi, L. Xu, N. M. Han, Q. Zheng, Y. W. Mai, J. K. Kim, *ACS applied materials & interfaces*, 10, 26641-26652.

59. L. Yao, Z. Pan, J. Zhai, H. H. Chen, *Nanoscale*, 2017, 9, 4255-4264.
60. D. Zhang, W. Liu, L. Tang, K. Zhou, H. Luo, *Applied Physics Letters*, 2017, 110, 133902.
61. L. Yao, Z. Pan, S. Liu, J. Zhai, H. H. Chen, *ACS applied materials & interfaces*, 2016, 8, 26343−26351.
62. R. Guo, H. Luo, W. Liu, X. Zhou, L. Tang, K. Zhou, D. Zhang, *Physical Chemistry Chemical Physics*, 2018, 20, 18031.
63. D. Zhang, W. Liu, R. Guo, K. Zhou, H. Luo, *Advanced Science*, 2018, 5, 1700512.